Seven-year monitoring of mercury in wet precipitation and atmosphere at the Amsterdam Island GMOS station

Antonella Tassone, Olivier Magand, Attilio Naccarato, Maria Martino, Domenico Amico, Francesca Sprovieri, Hippolyte Leuridan, Yann Bertrand, Michel Ramonet, Nicola Pirrone, et al.

Heliyon 9 (2023) e14608

Contents lists available at ScienceDirect

Heliyon

journal homepage: www.cell.com/heliyon

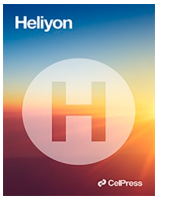

Research article

Seven-year monitoring of mercury in wet precipitation and atmosphere at the Amsterdam Island GMOS station

Antonella Tassone [a,*], Olivier Magand [b], Attilio Naccarato [a,c], Maria Martino [a], Domenico Amico [a], Francesca Sprovieri [a], Hippolyte Leuridan [d], Yann Bertrand [b], Michel Ramonet [d], Nicola Pirrone [a], Aurelien Dommergue [b]

[a] CNR-Institute of Atmospheric Pollution Research (CNR-IIA), Rende, Italy
[b] Institut des Géosciences de l'Environnement, Univ. Grenoble Alpes, CNRS, IRD, Grenoble INP, 38400, Grenoble, France
[c] Department of Chemistry and Chemical Technologies, University of Calabria, Via P. Bucci, Rende, Italy
[d] Laboratoire des Sciences du Climat et de l'Environnement, LSCE-IPSL (CEA-CNRS-UVSQ), Université Paris-Saclay, 91191, Gif-sur-Yvette, France

ARTICLE INFO

Keywords:
Wet deposition flux
Southern Hemisphere
Atmospheric pollution
Source identification
Atmospheric transport
Mercury measurements

ABSTRACT

Mercury (Hg) fate and transport research requires more effort to obtain a deep knowledge of its biogeochemical cycle, particularly in the Southern Hemisphere and Tropics that are still missing of distributed monitoring sites.

Continuous monitoring of atmospheric Hg concentrations and trend worldwide is relevant for the effectiveness evaluation of the Minamata Convention on Mercury (MCM) actions. In this context, Gaseous Elemental Mercury (GEM) and total mercury (THg) in precipitations were monitored from 2013 to 2019 at the Amsterdam Island Observatory (AMS - 37°48′S, 77°34′E) to provide insights into the Hg pathway in the remote southern Indian Ocean, also considering ancillary dataset of Rn-222, CO_2, CO, and CH_4. GEM average concentration was 1.06 ± 0.07 ng m^{-3}, with a slight increase during the austral winter due to both higher wind speed over the surface ocean and contributions from southern Africa. In wet depositions, THg average concentration was 2.39 ± 1.17 ng L^{-1}, whereas the annual flux averaged 2.04 ± 0.80 μg m^{-2} $year^{-1}$. In general, both GEM and Volume-Weighted Mean Concentration (VWMC) of THg did not show an increasing/decreasing trend over the seven-year period, suggesting a substantial lack of evolution about emission of Hg reaching AMS.

Air masses Cluster Analysis and Potential Source Contribution Function showed that oceanic evasion was the main Hg contributor at AMS, while further contributions were attributable to long-range transport events from southern Africa, particularly when the occurrence of El Niño increased the frequency of wildfires.

1. Introduction

Due to its toxicity and great impact on human health and the environment, mercury (Hg) has increasingly been investigated by the scientific community [1,2] with the overall aim to reduce its emissions in each environmental compartment [3]. The Minamata Convention on Mercury (MCM) is perhaps the most important international regulatory framework aimed at protecting human health

* Corresponding author. CNR-Institute of Atmospheric Pollution Research, Rende, Italy.
E-mail address: antonella.tassone@iia.cnr.it (A. Tassone).

https://doi.org/10.1016/j.heliyon.2023.e14608
Received 20 December 2022; Received in revised form 5 March 2023; Accepted 13 March 2023
Available online 18 March 2023

and the environment from anthropogenic emissions of Hg and its compounds [4] and the effectiveness evaluation of its actions has highlighted the need to increase the number of ground-based monitoring sites worldwide, particularly in areas of scarce data coverage and to provide comparable Hg data both in the background and in impacted areas [5]. This complex framework draws attention to the need for multiple analytical methods and the exploitation of new analytical strategies for comprehensive investigations, which should also include remote areas [6–9].

Although several Hg monitoring programs and networks have been established over the years [10–13], the monitoring stations that provide Hg data both in air and wet depositions in the open ocean and remote areas are still limited in number [8,10,14–24] particularly in the Southern Hemisphere.

In this context, the station on Amsterdam Island (AMS) has been set up in the framework of the Global Mercury Observation System (GMOS) Hg global network (http://www.gmos.eu/), with the support of the French Polar Institute (IPEV). The unique geographic location of this site has enabled the study of background data on major air pollutants in the Southern Hemisphere due to the absence of local anthropogenic sources and its distance from maritime traffic routes [15,17,25–29].

The present manuscript is an updated study on the temporal variability of Gaseous Elemental Mercury (GEM) and total Hg (THg) in precipitations from 2013 to 2019 at AMS providing new insights into the Hg pathway in the Southern Hemisphere. The investigation of seasonal and inter-annual variability, combined with the analysis of CO_2, CO, CH_4, and radon-222 (Rn-222) data, with the support of Potential Source Contribution Function (PSCF) and Cluster Analysis (CA), permitted to assess the evolutionary tendencies of Hg at the Southern Hemisphere midlatitudes and pinpoint the potential sources associated with long-range transport and El Niño Southern Oscillation (ENSO).

2. Materials and methods

2.1. Sampling site

Amsterdam Island (37.7983° S, 77.5378° E) is a small remote volcanic island of 55 km^2 in the southern Indian Ocean, 3200 km from Australia, 3400 km from Madagascar, 4200 km from South Africa, and 3300 km from Antarctica. The atmospheric observatory of Pointe Benedicte is northwest to the island at an altitude of 55 m above sea level, and due to its strategic position that ensures minimal local interference, the station is of particular interest to study Hg dynamics and pathway under unique background conditions.

Within the GMOS global network, it has been classified as a master site [11] and it is also part of other atmospheric monitoring programs such as the Global Atmosphere Watch World Meteorological Organization (GAW WMO), the French national monitoring system Integrated Carbon Observation System ICOS-France-Atmosphere for the long-term observation of greenhouse gases (GHGs), and the Global Observation System for Mercury (GOS^4M) GEO Flagship [10,16,17]. A more detailed description of the site is given in the Supporting Information (Text S1).

2.2. Meteorological variables and CO_2, CO, CH_4, and Rn-222 measurements

Meteorological data – air temperature, rainfall amount, wind speed and direction – were provided by the local meteorological station. The dataset of GHGs included CO_2, CO, and CH_4 from March 23, 2013, to December 22, 2019. A temporal gap exists in the CO measurements, which started from December 2, 2015. CO_2, CO, and CH_4 were monitored using Picarro gas analyzers, which used cavity ring-down spectroscopy to measure the gas concentration every 30 s with a precision (1 sigma confidence) for hourly measurements of 10 ppb, 1 ppb, and 0.3 ppb, respectively, in compliance with the specifications of the manufacturer. Calibration was performed monthly. The raw data were manually checked and validated by ICOS staff [30], before being hourly averaged.

Radon-222 measurements, covering the same period considered for GHGs, were performed using an alpha spectrometer which required monthly calibration and ensured a minimum detected activity of about 10 mBq m^{-3} with an uncertainty of about 40%.

This set of ancillary data proved useful to track continental air over the ocean [31]. Indeed, Rn-222 concentration at AMS exceeding the threshold of 80 mBq m^{-3} (i.e., radonic storms), indicated that the air mass over the island recently passed over the mainland, usually southern Africa [17,32].

The time series of all gases were analyzed on an hourly, seasonal, and annual basis, with seasonal boundaries defined as follows: austral winter from July to September, austral summer from December to February, Intermediate Season 1 (IS1) from March to June, and Intermediate Season 2 (IS2) from October to November. This classification revealed useful since the meteorological conditions in June are more similar to that in the preceding months than in July–August, as also the case of other sites in the Southern Hemisphere, and more strictly in Africa [33].

2.3. Mercury determination in the atmosphere and wet deposition

2.3.1. GEM measurements

GEM was continuously measured from March 23, 2013, to December 22, 2019, using Tekran analyzer 2537A/B models (Tekran Inc., Toronto, Canada) based on amalgamation onto dual gold cartridge design, thermal desorption, and quantification by cold vapor atomic fluorescence spectroscopy (CV-AFS). Calibration was performed using both the internal permeation sources (every 69 h) and manual injections of saturated Hg vapor (every year). To ensure comparability of the Hg data, GEM measurements were carried out according to GMOS Standard Operating Procedures (SOPs) [34].

2.3.2. Rainwater sampling and total mercury quantification

Wet deposition samples were continuously collected from March 24, 2013, using an automatic wet-only NSA-171 Eigenbrodt collector which comprises a glass funnel connected to a 1-L fluorinated high-density polyethylene (FLPE) bottle. The entire sampling apparatus was thoroughly acid-cleaned, according to the procedures reported by Tassone et al. [35], based on the SOPs developed within the GMOS network [36]. Each deployment lasted 6–45 days, depending on the season (wet or dry) and according to exceptional periods of intense rainfall events. Analyses of wet deposition samples were performed at the CNR-IIA laboratories following the US-EPA method 1631E guidance reported in the literature [35]. Quality assurance/quality control (QA/QC) procedures were routinely implemented, including the analysis of duplicate samples, accuracy test using certified reference material (NIST1641), matrix spikes, and assessment of Hg contamination through the analysis of the system, transport, reagent and field blanks (more details in Text S2).

2.4. Data treatment

Raw GEM time series were quality-controlled according to GMOS SOPs, using a dedicated software developed at the Institute of Environmental Geosciences (https://doi.org/10.25326/168 available at https://gmos.aeris-data.fr, last access: February 10, 2023) [37]. Specifically, the QA/QC procedure involved comparing the raw data with fixed criteria, concerning both the calibration and the readout steps of airborne measurements [34].

THg values were derived according to UNI 15853:2010 and converted into volume-weighted mean concentration (VWMC) values, while seasonal and annual Hg wet deposition fluxes (F_w) were calculated as reported in Sprovieri et al. [10] by using the seasonal/yearly VWMCs and cumulative rain depths (P^i, mm), according to Eq. (1):

$$F_w = VWMC_{Hg} \sum_{i=1}^{n} P^i / 1000 \quad (1)$$

The statistical significance of temporal variability of each variable was determined using linear regression with the method of Pearson's correlation coefficient and the differences in annual and seasonal concentration values were investigated using Mann-Whitney and ANOVA tests.

The seasonal Mann-Kendall trend test was applied to monthly mean data of each variable, after verification of their significant seasonality using the Kruskal-Wallis test, to detect trends while Sen's slope estimator was applied to assess their magnitude, using the Theil-Sen method [38].

The investigation of the impact of El Niño on Amsterdam Island was conducted using cross-correlation to seek lag times between the Southern Oscillation Index (SOI), as a tracer of El Niño occurrence, and GEM and CO concentrations. All data analyses were performed using the R software.

2.5. Backward trajectories and source identification techniques

The interpretation of the surveyed time series was carried out using the U.S. NOAA's HYbrid Single-Particle Lagrangian Integrated Trajectory (HYSPLIT) model (http://ready.arl.noaa.gov/HYSPLIT.php, last access: May 3, 2022), which permitted to obtain information on the path of air masses to the receptor site. For this purpose, the READY website was used to compute 5-day back-trajectories, at 3-h intervals, at 50 m above ground level in the domain 70°–0° S and 0°–120° E [33,39,40]. Considering the remoteness of the island, 5-day trajectories may be deemed short for tracing possible Hg sources reaching AMS. However, longer trajectories calculated for the entire 7-year monitoring period would have entailed a higher computational cost. We therefore calculated 10-day trajectories only for few cases, in order to support our findings overcoming computational limitations. More specifically, 10-day trajectories were used to facilitate the interpretation of particularly high or low values of GEM and Rn as well as to run the CA. The GDAS 1° × 1° from the Global Data Assimilation System was selected as the meteorological dataset [41].

In addition, CA was applied to group air masses according to their origin through the computation of the proportion of time that a particular back-trajectory was in a specific wind sector (e.g., S, SW, W). CA was performed using Ward's Minimum-Variance method which, starting with groups containing single trajectories, iteratively merges pairs of them so as to obtain the minimum increase in the sum of squared distances between the members and the centroids of the corresponding groups, summed over the resulting groups [42–44]. The centroid of the newly-formed group, i.e., our mean trajectory, is recomputed each time using the data from the individual groups previously separated, before calculating the squared distances [45]. In our study, an angle distance matrix was used to assess the similarity between the trajectories to be merged. The optimal number of clusters was chosen following the total spatial variance (TSV) metric in the Elbow method [45,46], selecting a variance criterion of 20%. This approach relies on calculating the sum of the spatial variance of all the clusters, until TSV increases significantly, thus indicating that the merged clusters are not very similar. This increase in TSV denotes the completion of the clustering process [47], and in our case, it resulted in four clusters as the optimal number. Furthermore, a hybrid receptor model, namely the Potential Source Contribution Function, was used to locate potential emission sources around the receptor site [48,49]. This technique assumes that air masses that intercept emission sources in the grid cell (i, j) can get enriched in the pollutants emitted by that source and transport them to the receptor site. The PSCF is defined by Eq. (2):

$$PSCF = \frac{m_{ij}}{n_{ij}} \quad (2)$$

where n_{ij} is the number of times that the trajectories passed through the cell and m_{ij} is the number of times that a source concentration was high (>90th percentile) when the trajectories passed through the cell (i, j). The cell with the higher PSCF value thereby characterizes the most likely source location.

3. Results and discussion

3.1. Variability of CO_2, CO, CH_4, Rn, and meteorological conditions

The summary of the annual meteorological variables and atmospheric gases is listed in Table 1. The monthly median air temperature ranged from 11 °C in winter to 19 °C in summer (Fig. S1) while winds mainly blew from NNW to WSW, without significant differences in direction among the seasons (Fig. S1), except for a higher frequency of N-NW air masses during winter. The most abundant precipitations were measured during IS1 except for 2013, when the maximum was recorded during winter (Fig. 1). On an annual basis, rainfall averaged 905 ± 62 mm and varied between 833 mm, collected in 2013, and 1003 mm, in 2019.

The measured CO_2 (n = 56976, 89.5% of available hourly data) showed a statistically significant increase over the investigated period, from 390.5 ppm in 2013 to 412.8 ppm in 2019 (Fig. S2), with an average rate of 2.46 ppm $year^{-1}$ ($p < 0.05$), thus confirming the growing trend already found in previous studies [26]. Daily CO_2 concentration showed little variability among the seasons, with a slight decrease between 9 a.m. and 6 p.m., suggesting a weak influence from the photosynthetic activity of local vegetation (Fig. S2).

The hourly CO values (n = 34264, 88% of available data) ranged from 30 ppb to a maximum of 65 ppb (Fig. S3), with an upward significant trend ($p < 0.05$), as confirmed by the positive Sen's slope value, which was 6.8e-05 ppb $year^{-1}$. However, it is worth noticing that this increasing tendency was very small, thus not physically meaningful. On a seasonal basis, a clear distribution was observed, with the lowest values being obtained in February and March (Fig. S3), due to removal phenomena favored by the high presence of radical OH during IS1. Conversely, these removal processes were weak during winter and the CO concentration increased significantly, with maxima in October [50]. In addition, between June and October, this pattern was probably influenced by the long-range transport of CO released during the biomass burning events in southern Africa [51].

The hourly CH_4 values (Fig. S4) showed a statistically significant increase from 1747 ppb to 1841 ppb with an average value of 1794 ± 21 ppb (n = 56964, 89.5% of available hourly data) and a growth rate of 8.5 ppb $year^{-1}$ ($p < 0.05$). The lowest values were recorded in January–April (Fig. S4) and were mainly due to the reaction with OH radicals, as was also observed for CO. Indeed, CH_4 and CO showed a significant correlation ($r = 0.57$, $p < 0.05$) over the covered period, suggesting that common mechanisms have driven their pattern on a seasonal scale [50,52,53].

The 2-h Rn-222 activity was on average 35.36 ± 32.24 mBq m^{-3} (n = 26988, 92.3% of available data) with a maximum of 398.80 mBq m^{-3} (Fig. S5). The Mann-Kendall test revealed a significant decrease that was confirmed by the Sen's slope value (−4.1e-04 mBq m^{-3} $year^{-1}$). However, this tendency was quite small, therefore not physically meaningful, as in the case of CO. Annual Rn activities (Fig. S5) ranged between 24.93 ± 26.78 mBq m^{-3} (in 2016) and 48.10 ± 19.4 mBq m^{-3} (in 2013), as typical for marine air masses which usually range between 30 and 50 mBq m^{-3} [27,54,55]. Radonic storms from southern Africa were mainly detected during winter (Fig. S5), which is the season with the greatest contribution of the long-range transport [17]. Their continental origin was confirmed by the correlation between Rn and CO, which improved when considering only the biomass burning season (i.e., austral winter) rather than the entire period, with a 10-fold increase in the correlation coefficient, from 0.02 to 0.20 ($p < 0.05$). Besides, by looking at the relationship between Rn and wind direction (Fig. S5), it can be noticed a lower frequency of radonic storms transported up to AMS during the second half of the investigated period. Although there was substantial uniformity in the direction of Rn origin (WNW), these radonic storms decreased their frequency from W over time, and in 2019 they were recorded only from the northernmost (NW) sectors.

Table 1
Annual mean (± standard deviation) of the meteorological variables and monitored gases, namely CO_2, CO, Rn-222, CH_4, and Gaseous Elemental Mercury (GEM) at AMS from March 2013 to December 2019. Annual mean (± standard deviation) of volume-weighted mean concentration (VWMC) of total mercury in rainwater and wet deposition fluxes are also reported.
(n.a. = not available).

	Temperature (°C)	Rainfall (mm)	CO_2 (ppm)	CO (ppb)	Rn-222 (mBq m^{-3})	CH_4 (ppb)	GEM (ng m^{-3})	VWMC (ng L^{-1})	Wet deposition flux (μg m^{-2} $year^{-1}$)
2013	13.7 ± 2.2	833	393.4 ± 0.8	n.a.	48.1 ± 19.4	1769 ± 11	1.04 ± 0.09	2.34 ± 0.93	1.95 ± 0.15
2014	14.2 ± 2.8	864	395.2 ± 0.9	n.a.	41.7 ± 14.2	1774 ± 15	1.05 ± 0.06	1.80 ± 1.07	1.55 ± 0.33
2015	14.4 ± 2.8	916	397.5 ± 0.9	50.0 ± 3.3	46.8 ± 13.4	1786 ± 14	1.02 ± 0.07	1.16 ± 0.30	1.06 ± 0.13
2016	14.5 ± 2.9	967	400.7 ± 1.0	52.1 ± 6.7	24.1 ± 8.3	1792 ± 12	1.08 ± 0.06	3.04 ± 1.39	2.94 ± 0.44
2017	15.0 ± 2.9	894	402.7 ± 0.9	45.2 ± 6.8	32.0 ± 7.5	1799 ± 15	1.02 ± 0.08	2.18 ± 1.63	1.95 ± 0.31
2018	14.8 ± 3.3	855	405.2 ± 0.9	42.8 ± 8.1	31.1 ± 8.8	1810 ± 14	1.08 ± 0.05	4.67 ± 3.95	3.31 ± 0.58
2019	14.3 ± 3.0	1003	407.6 ± 1.1	50.5 ± 7.8	26.9 ± 7.1	1817 ± 13	1.08 ± 0.06	1.55 ± 0.47	1.55 ± 0.26

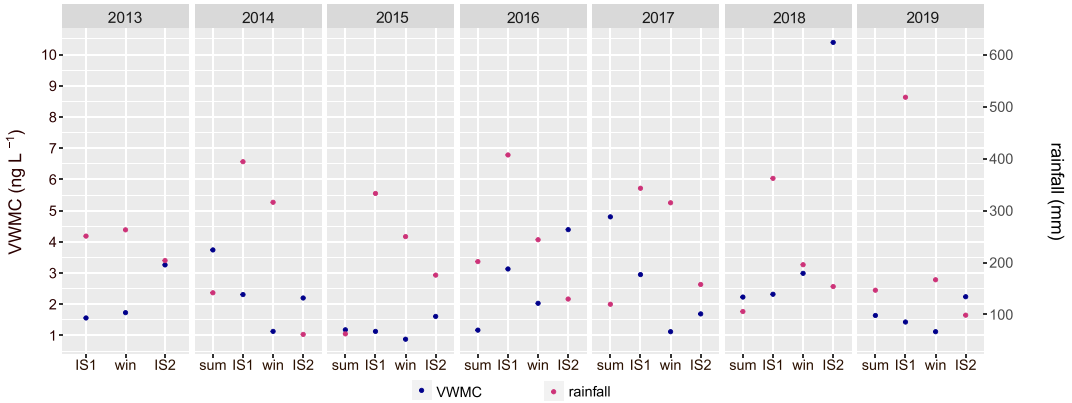

Fig. 1. The plot of the seasonal volume-weighted mean concentration (VWMC) of total mercury in rainwater and rainfall amount in the 2013–2019 period (IS1 = M-A-*M*-J; austral winter = J-A-S; IS2 = *O*–N; austral summer = D-J-F).

3.2. Hg in the atmosphere and wet deposition

3.2.1. GEM measurements

The individual mean hourly GEM values from March 2013 to December 2019 (Fig. 2) ranged from 0.70 to 1.58 ng m^{-3}, resulting in a mean concentration of 1.06 ± 0.07 ng m^{-3} (n = 45018, 70.7% of available data), which is comparable with the concentrations (0.9–1.0 ng m^{-3}) usually found at background sites of the Southern Hemisphere [11]. The observed GEM was also consistent with previous measurements at AMS, which reported concentrations of 1.03 ng m^{-3} [17] and 1.05 ng m^{-3} [16], as well as at the Cape Point station in southern Africa, where the annual mean GEM was 1.09 ng m^{-3} [16]. However, concentrations at AMS were slightly higher than in other subequatorial sites, such as the EMMA station in Argentina, where the average concentration was 0.9 ng m^{-3} [22], and the Cape Grim station in Tasmania, where concentrations of 0.9–1.0 ng m^{-3} were found [56,57]. On a seasonal basis (Fig. 2), we recorded a slightly but significantly higher Hg concentration in winter than in summer (1.08 ± 0.05 vs. 1.06 ± 0.07 ng m^{-3}, $p < 0.05$). This seasonal variability may be ascribed to the impact of the Intertropical Convergence Zone (ITCZ) shift during the austral winter, which caused changes in the wind speed on the sea surface [58], thus favoring Hg emission. Indeed, ITCZ is a belt of air masses from both the Northern and Southern hemispheres mixing together which crosses the equator from south to north around April–May (IS1) and reaches its northernmost point around June–July (winter), and then moves south again around August-September [58,59]. Therefore, the relocation of the ITCZ over the Indian Ocean was likely a vector of air masses from the north to AMS that reasonably influenced the recorded GEM concentrations. In addition, a non-negligible contribution to the observed GEM seasonal variability was the long-range transport from southern Africa during the biomass burning season, that was confirmed by the significant positive correlation between GEM and CO only in winter ($r = 0.28$, $p < 0.05$), contrary to the findings regarding the correlations between GEM and CO_2 or CH_4, which were in all cases non-significant.

3.2.2. Total mercury in rainwater

The annual-averaged VWMC of THg in precipitation samples (n = 27) was 2.39 ± 1.17 ng L^{-1} and varied in the range from 1.16 ng L^{-1} to 4.67 ng L^{-1}, which were obtained in 2015 and 2018, respectively, when total rainfall was 916 mm and 855 mm (Table 1 and Fig. 1). On both a seasonal and annual basis, the VWMC showed no significant increase or decrease over time, suggesting that no substantial changes in the concentration of atmospheric oxidized Hg species during the investigated period were observed. Since a significant source of these species at AMS is biomass burning in southern Africa [16], it can be hypothesized that these emissions did not change during the last decade.

Even focusing only on the winter seasons, when African air masses are detectable at AMS, we did not observe a clear upward/

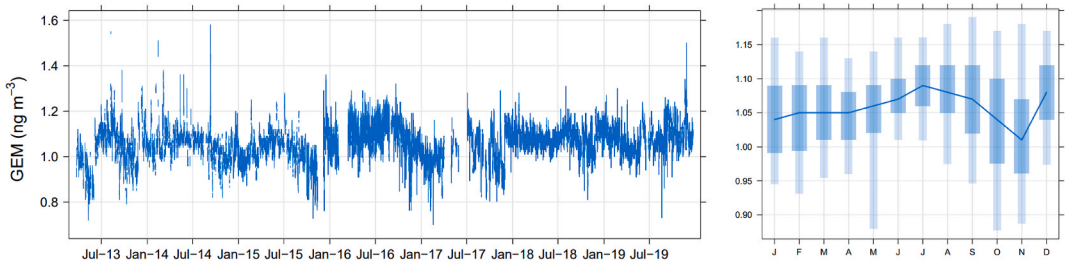

Fig. 2. Temporal variability of Gaseous Elemental Mercury (GEM) from March 2013 to December 2019: Individual hourly mean values (left panel) and monthly median values (right panel). The shadings in the monthly median plot represent 25/75th and 5/95th quantile values.

downward tendency of VWMC, rather it was mostly fluctuating (Fig. 1). Except for 2016, the lowest values were observed during the rainy season, i.e., from May to October, due to the movement of cold fronts from the west. Conversely, higher values were mainly found in IS2 (Fig. 1), except for 2014 and 2017 when a peak was recorded during summer. In particular, during IS2 2018 we observed a VWMC value of 10.93 ng L^{-1}, associated a rainfall amount (199 mm) that was not notably different from the typically measured values. The analysis of the wind roses combined with backward trajectories during IS2 2018 did not provide us with immediate answers to this event. Within the same synoptic pattern, more intense winds from the W and WNW sectors in IS2 than other seasons were recorded (Fig. S6), suggesting the potential contribution of long-range transport from Africa. Therefore, we hypothesize during this season some unusual emission phenomena occurred in Africa, whose oxidized Hg was then scavenged by the wet deposition reaching AMS [60,61]. This hypothesis is supported by previous measurements at AMS, which showed that the highest concentrations of particle-bound Hg were observed during episodes of stronger winds from the NW sector [17].

The effect of washout of atmospheric oxidized Hg species from wet deposition was studied on a seasonal basis by correlating VWMC with total rainfall ($n = 27$, $r = -0.21$, $p > 0.05$) (Fig. 3), which resulted in a negative but not significant coefficient. The correlation was low because the occurrence was observed by considering seasonal values from samples that averaged out their respective contributions. Similarly, a non-significant correlation was found between GEM and wet deposition volume ($n = 27$, $r = 0.11$, $p > 0.05$), suggesting rainfall events did not affect GEM concentration (Fig. 3). As regards the VWMC and the corresponding seasonal GEM concentrations (Fig. 3), the correlation study revealed a not significant linear relationship between the two forms ($n = 27$, $r = 0.05$, $p > 0.05$), which was probably due to their different temporal variability. Indeed, GEM showed a quite stationary pattern compared to the more variable VWMC throughout the covered period.

The values of VWMC in precipitation samples and their respective precipitation volumes resulted in an average wet deposition flux of 2.04 ± 0.80 μg m^{-2} $year^{-1}$, and therefore slightly higher than the value of 1.95 μg m^{-2} $year^{-1}$ reported in a previous study [10]. This finding was impacted by the higher value of Hg in wet deposition observed in 2018. In fact, during 2018 the highest wet deposition flux was attained (3.31 μg m^{-2} $year^{-1}$), whereas the lowest value (1.06 μg m^{-2} $year^{-1}$) resulted in 2015. On a seasonal scale, the maximum flux varied year-to-year between IS1 and IS2.

A positive significant correlation ($n = 27$, $r = 0.48$, $p < 0.05$) was observed between the wet deposition flux and associated rainfall (Fig. 3), indicating that wet Hg deposition flux increased with increasing rainfall, as also reported in other studies showing that rainfall had a greater influence on the variation of wet deposition fluxes [62].

The average THg (whence the HgII forms) wet deposition flux is lower than the GEOS-Chem model results that produced wet Hg deposition flux around 5–6 μg m^{-2} $year^{-1}$ [63,64] in the areas surrounding AMS. Compared with other models, such as GLEMOS, GEM-MACH-Hg, and ECHMERIT, our experimental result was also lower, as can be seen from the spatial distribution maps reported in Travnikov et al. [65], from which it can be inferred that the flux value in 2013 ranged in 2.9–4.4, 2.9–7.3, and 4.4–7.3 μg m^{-2} $year^{-1}$, respectively. This model-to-measurement gap outlines the importance of monitoring wet deposition at AMS to gather experimental results that contribute to the study of the latitudinal gradient of HgII wet deposition over the oceans, hence improving the

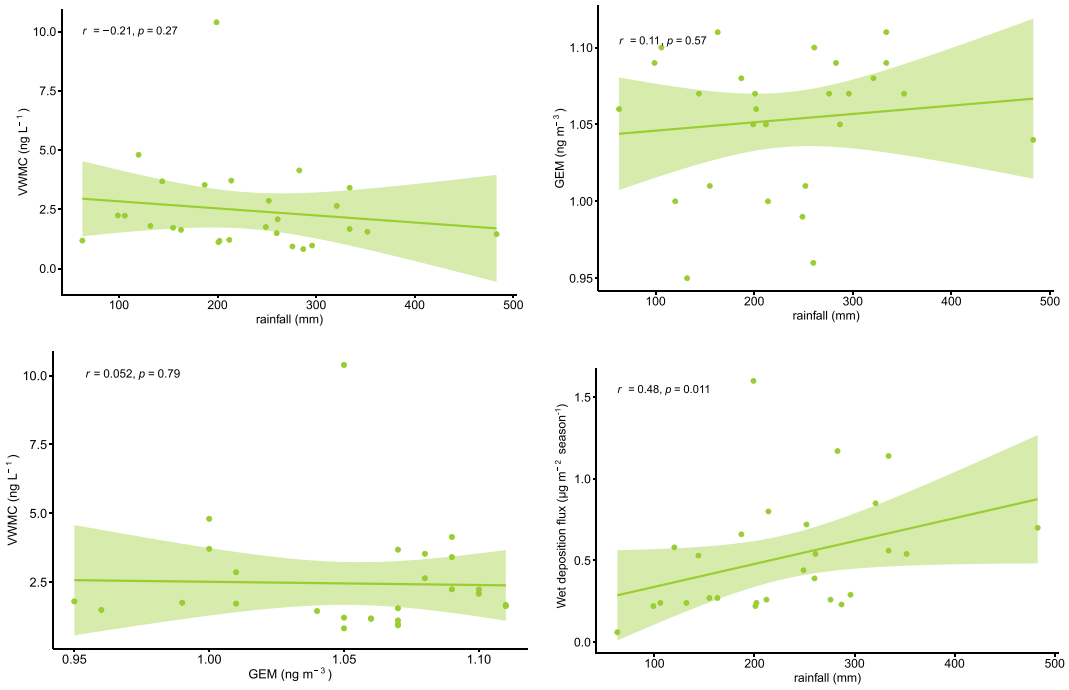

Fig. 3. Correlation plots of seasonal averages of VWMC versus total rainfall (upper left); GEM versus total rainfall (upper right); VWMC versus GEM (lower left); Wet deposition flux versus rainfall (lower right).

understanding of Hg inputs to different ocean regions.

3.3. Influence of the El Niño Southern Oscillation (ENSO)

The El Niño Southern Oscillation (ENSO) is a cyclical meteorological event that occurs approximately every 3–7 years and causes variation of rainfall amount with consequent impact on emission phenomena, such as biomass burning due to long periods of drought [66–68]. The occurrence of El Niño has usually been detected using atmospheric indexes like SOI (Southern Oscillation Index), MEI (Multivariate ENSO Index), and ONI (Oceanic Niño Index).

From 2013 to 2019 (Fig. 4), ONI values reached very high levels between July 2015 and July 2016, with a peak in December–January. MEI and SOI also showed a very similar, increasing trend over the same period. However, the growth of all the indexes around 2016 was not accompanied by a sharp and direct increase in GEM, suggesting at first a limited simultaneous influence of ENSO. On the contrary, the highest GEM concentrations were observed at the most negative SOI values on average 6–8 months after the El Niño event (Fig. S7). This result is in agreement with the findings at Cape Point (South Africa) and Mace Head (Ireland) [67], therefore supporting the influence of El Niño on GEM variability, which can occur with the increased wildfire frequency (which also impacts CO concentration) [67] or with enhanced Hg re-emission from the ocean surface caused by the increase of the sea surface temperature [69, 70]. Huang and Zhang indeed recently simulated by GEOS-Chem model a positive anomaly of atmospheric Hg concentration, lagged of 3 months, driven by Hg(0) evasion fluxes after the occurrence of El Niño [71].

In our study, we found a significant cross correlation between CO and SOI, with lag time peaking at 4–6 months (Fig. S7) comparable to that between GEM and SOI and therefore we suggest that ENSO-modulated biomass burning was one of the major mechanisms of GEM variability on Amsterdam Island.

3.4. Backward trajectories analysis

The analysis of the 10-day backward trajectories revealed that more than 30% of the GEM peaks (concentration>95th percentile) were associated with the transport of air masses coming from southern Africa during the biomass burning season (Fig. S8). A similar apportionment was confirmed for the high concentrations of Rn-222 (Fig. S8), whose pattern was mainly affected by the emissions from the African continent. The 10-day trajectory analysis was also useful to analyze low GEM concentrations, which were mainly linked to southerly polar air masses (Fig. S8), and low Rn values, which were also traced to air masses traveling over the ocean from the Antarctic (Fig. S8), which has low local emissions of Rn, being almost entirely covered by ice [72].

For each individual year, the analysis of 5-day backward trajectories reaching AMS revealed no particular differences on both annual and seasonal scales (Fig. S9), although differences could be expected on a seasonal basis at least for the summer of 2016 because of the occurrence of El Niño.

The four clusters of the 10-day backward trajectories resulting from the CA were clearly associated with the marine environment, though coming from different sectors: The first cluster (C1) collected a set of trajectories coming from *N*-NNE; the second (C2) and fourth (C4) clusters those coming from the SW, probably intercepting masses also from the subantarctic and Antarctic region, while the third (C3) from the NW sector collected trajectories probably intercepting masses near the African continent (Fig. S10). These results

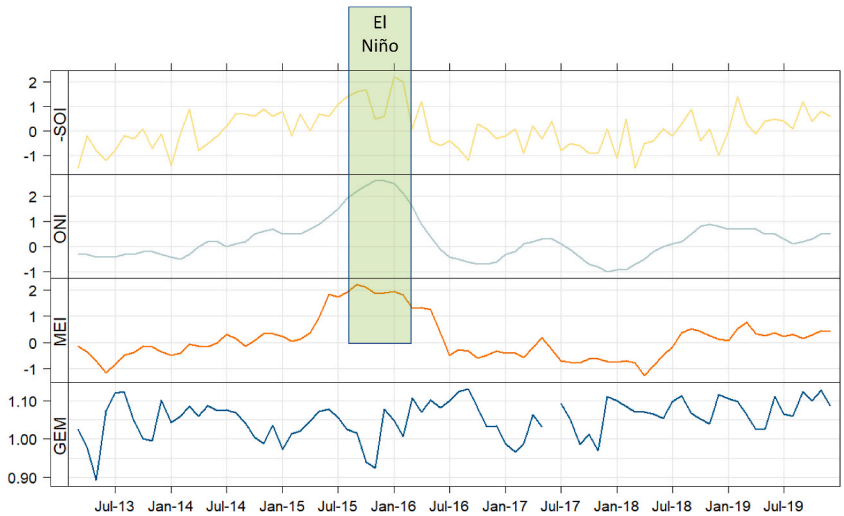

Fig. 4. Temporal plot of the SOI, ONI, MEI indexes during the monitored period useful to assess ENSO occurrence and trend of GEM over the same period. (For a better visualization, SOI was sign-changed using multiplication by −1). The exceedance of the threshold of ±0.5 °C of the ONI for five consecutive months is used as evidence of El Niño (+0.5 °C), as well as large positive values of –SOI and MEI. The light green box indicates the occurrence of the El Niño. (For interpretation of the references to colour in this figure legend, the reader is referred to the Web version of this article.)

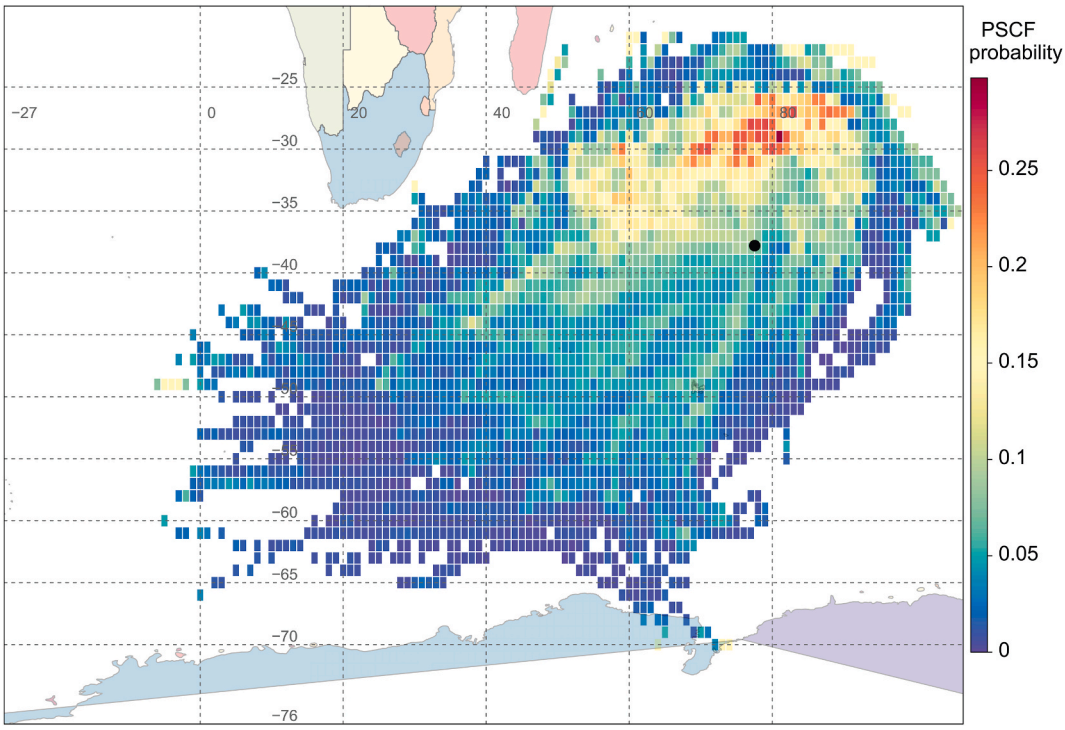

Fig. 5. The plot of the PSCF probabilities for GEM concentrations (90th percentile) at AMS in the 2013–2019 period. The round black dot indicates the location of Amsterdam Island.

allowed us to demonstrate that air masses reaching AMS essentially traveled over the ocean, so we could assume that the origin of Hg was related to the marine environment with occasional continental sources. This outcome agrees with the literature on pollutant load at this site, which reports oceanic emissions and biomass burning as the pathways that primarily influence the occurrence of pollution events.

The results of the CA were combined with the maps obtained from the PSCF technique for GEM and Rn-222, thus obtaining indications about the most likely source location of these two pollutants. The map obtained for GEM over the entire 2013–2019 period showed that the highest values of GEM were associated with clusters C1 and C3 (Fig. 5), thus supporting our hypothesis that the main contribution to GEM concentration was the emission from the subtropical ocean, which contributed to depositional fluxes, as expected for marine regions [10]. The second GEM source was probably of continental origin, arising from WNW air masses that crossed through some areas of southern Africa, meeting the assumption of the influence of long-range transport on the pollution load on Amsterdam Island. The detailed study of the PSCF maps by season did not show significant differences in the PSCF probability, except for C1 where the highest values of this probability were found during summer and IS2, two periods with higher solar radiation and temperature gradient in the air-water interface that favor the emission of elemental Hg from surface water [73]. As for the lower GEM values, the PSCF confirmed the limited contribution that southerly polar air masses (C4 and C2 clusters) provided to the GEM concentration at AMS. In summary, our findings suggested GEM levels on Amsterdam Island are consistent with primary control by evasion from subtropical marine waters and transport from the African continent. Besides, considering the lack of upward/downward trend in both GEM and VWMC, we can surmise that there has been no evolution in the Hg emissions intercepted at AMS from Africa.

A different situation was found with Rn, for which the PSCF map in the entire period showed a higher probability associated with cluster C3 (Fig. S11), also providing further evidence that the cluster C3 was associated with trajectories coming from southern Africa. In addition, observation of the seasonal PSCF maps clarified that Rn sourced most probably from the African inland in winter and was transported to AMS (Fig. S11). In support of this conclusion, previous studies of air mass backward trajectories ending at AMS and Rn measurements showed that southern Africa (including Madagascar) was the predominant non-marine source of trace materials transported to AMS [27,74,75].

4. Conclusions

Given the importance of Hg pollution control on a global scale, continuous measurements have been carried out at the station on Amsterdam Island, a unique monitoring site in the Indian Ocean.

The GEM concentration throughout 2013–2019 was quite stationary, ranging from 0.70 to 1.58 ng m^{-3}, with an average value of 1.06 ± 0.07 ng m^{-3}, following the typical background concentrations in the Southern Hemisphere. The highest values were recorded during winter, presumably due to the ITCZ variability that caused higher wind speed over the surface ocean, and the long-range

contribution of biomass burning from South Africa. In addition, the occurrence of the El Niño in 2016 led to GEM peaks which were detected at AMS with a delay of 6–8 months.

Statistical tools such as CA and PSCF showed that oceanic emission was the major driver of GEM, while Rn-222 at AMS was primarily associated with long-range transport from southern Africa. In precipitation, the VWMC of THg was 2.39 ± 1.17 ng L^{-1} on average and varied between 1.16 and 4.67 ng L^{-1}, which corresponded to wet deposition fluxes between 1.06 and 3.31 μg m^{-2} $year^{-1}$. However, the substantial lack of increasing/decreasing trend for both GEM and VWMC suggested that there was no clear evolution about emission of Hg transported to AMS from Africa, hence numerous efforts still need to be made for an effective long-term reduction of the concentration of this pollutant to fulfill the objectives of the MCM.

Credit authors statement

Antonella Tassone: Conceptualization of the study, preparation of material for sampling, laboratory Hg analysis, data analysis, original manuscript writing; **Olivier Magand**: Implementation of Hg measurements at TAAF-IPEV Amsterdam Island district, observations monitoring management, field campaign, data treatment qualification and validation, IPEV GMOStral-1028 and Hg dataset AERIS (GMOS-FR national database https://gmos.aeris-data.fr/) program managing, funding acquisition, original manuscript writing; **Attilio Naccarato**: Conceptualization of the study, supervision and coordination of the work, original manuscript writing, funding acquisition and project managing; **Maria Martino**: Preparation of material for sampling, laboratory Hg analysis, data analysis; **Domenico Amico**: Preparation of material for sampling, laboratory Hg analysis, data analysis; **Francesca Sprovieri**: Manuscript review and editing, funding acquisition and project managing, GMOS network coordination; **Hippolyte Leuridan**: ICOS station management at Amsterdam Island; **Yann Bertrand**: IPEV GMOStral-1028 field campaign on THg in precipitation; THg collector system maintenance; **Michel Ramonet:** ICOS station management at Amsterdam Island; **Nicola Pirrone**: Funding acquisition and project managing, GMOS network coordination; **Aurelien Dommergue**: Implementation of Hg measurements at TAAF-IPEV Amsterdam Island district, funding acquisition. All co-authors contributed to data interpretation, reviewing, and editing the manuscript.

Funding

The authors from CNR-IIA would like to acknowledge the contribution received from the following projects.

- FET Proactive project “Towards new frontiers for distributed environmental monitoring based on an ecosystem of plant seed-like soft robots” (I-Seed). This project has received funding from the European Union’s Horizon 2020 research and innovation programme under grant agreement No 101017940.
- EMPIR - EURAMET project “Metrology for traceable protocols for elemental and oxidized mercury concentrations” (SI–Hg); grant no. 19NRM03. This project (SI–Hg) has received funding from the EMPIR programme co-financed by the Participating States and from the European Union’s Horizon 2020 research and innovation programme.
- Amsterdam Island GEM data, accessible in GMOS-FR national database (https://gmos.aeris-data.fr/) have been collected with funding from European Union 7th Framework Programme project Global Mercury Observation System (GMOS 2010–2015), the French Polar Institute IPEV via GMOStral-1028 IPEV program since 2012, the LEFE CHAT CNRS/INSU (TOPMMODEL program) and the H2020 ERA-PLANET (689443) iGOSP programme.

Data availability statement

Data associated with this study has been deposited at https://gmos.aeris-data.fr/.

Declaration of interest’s statement

The authors declare no conflict of interest.

Acknowledgments

We deeply thank all overwintering staff at AMS and the French Polar Institute Paul-Emile Victor (IPEV) staff and scientists who helped with the setup and maintenance of the experiment at AMS in the framework of the GMOStral-1028 IPEV program. AMS GEM data were collected via instruments coordinated by the IGE-PTICHA technical platform dedicated to atmospheric chemistry field instrumentation. The authors acknowledge the AERIS data infrastructure for providing access to the GEM data in this study.

We thank Dr. Gianluca Bevacqua from the Language Centre of the University of Calabria and CNR-IIA for the English proofreading of the manuscript.

Appendix A. Supplementary data

Supplementary data to this article can be found online at https://doi.org/10.1016/j.heliyon.2023.e14608.

References

[1] H. Zhang, S. Wu, E.M. Leibensperger, Source-receptor relationships for atmospheric mercury deposition in the context of global change, Atmos. Environ. 254 (2021), 118349, https://doi.org/10.1016/j.atmosenv.2021.118349.

[2] F. Ciani, V. Rimondi, P. Costagliola, Atmospheric mercury pollution: the current methodological framework outlined by environmental legislation, Air Qual. Atmos. Heal. 14 (2021) 1633–1645, https://doi.org/10.1007/s11869-021-01044-4.

[3] Global UNEP, Mercury Assessment 2018, UNEP - UN Environment Programme, 2018 accessed April 19, 2021), https://www.unep.org/resources/publication/global-mercury-assessment-2018.

[4] UNEP, Minamata Convention on Mercury - Text and Annexes, UNEP, 2013, p. 69, 2013a.

[5] H. Selin, S.E. Keane, S. Wang, N.E. Selin, K. Davis, D. Bally, Linking science and policy to support the implementation of the Minamata Convention on Mercury, Ambio 47 (2018) 198–215, https://doi.org/10.1007/s13280-017-1003-x.

[6] D. Amico, A. Tassone, N. Pirrone, F. Sprovieri, A. Naccarato, Recent applications and novel strategies for mercury determination in environmental samples using microextraction-based approaches: a review, J. Hazard Mater. 433 (2022), 128823, https://doi.org/10.1016/j.jhazmat.2022.128823.

[7] A. Naccarato, A. Tassone, F. Cavaliere, R. Elliani, N. Pirrone, F. Sprovieri, A. Tagarelli, A. Giglio, Agrochemical treatments as a source of heavy metals and rare earth elements in agricultural soils and bioaccumulation in ground beetles, Sci. Total Environ. 749 (2020), 141438, https://doi.org/10.1016/j.scitotenv.2020.141438.

[8] A. Naccarato, A. Tassone, M. Martino, R. Elliani, F. Sprovieri, N. Pirrone, A. Tagarelli, An innovative green protocol for the quantification of benzothiazoles, benzotriazoles and benzosulfonamides in PM10 using microwave-assisted extraction coupled with solid-phase microextraction gas chromatography tandem-mass spectrometry, Environ. Pollut. 285 (2021), 117487, https://doi.org/10.1016/j.envpol.2021.117487.

[9] A. Naccarato, A. Tassone, M. Martino, S. Moretti, A. Macagnano, E. Zampetti, P. Papa, J. Avossa, N. Pirrone, M. Nerentorp, J. Munthe, I. Wängberg, G. W. Stupple, C.P.J.J. Mitchell, A.R. Martin, A. Steffen, D. Babi, E.M. Prestbo, F. Sprovieri, F. Wania, A field intercomparison of three passive air samplers for gaseous mercury in ambient air, Atmos. Meas. Tech. 14 (2021) 3657–3672, https://doi.org/10.5194/amt-14-3657-2021.

[10] F. Sprovieri, N. Pirrone, M. Bencardino, F. D'Amore, H. Angot, C. Barbante, E.-G. Brunke, F. Arcega-Cabrera, W. Cairns, S. Comero, M. del C. Diéguez, A. Dommergue, R. Ebinghaus, X. Bin Feng, X. Fu, P.E. Garcia, B.M. Gawlik, U. Hageström, K. Hansson, M. Horvat, J. Kotnik, C. Labuschagne, O. Magand, L. Martin, N. Mashyanov, T. Mkololo, J. Munthe, V. Obolkin, M. Ramirez Islas, F. Sena, V. Somerset, P. Spandow, M. Vardè, C. Walters, I. Wängberg, A. Weigelt, X. Yang, H. Zhang, Five-year records of mercury wet deposition flux at GMOS sites in the Northern and Southern hemispheres, Atmos. Chem. Phys. 17 (2017) 2689–2708, https://doi.org/10.5194/acp-17-2689-2017.

[11] F. Sprovieri, N. Pirrone, M. Bencardino, F. D'Amore, F. Carbone, S. Cinnirella, V. Mannarino, M. Landis, R. Ebinghaus, A. Weigelt, E.G. Brunke, C. Labuschagne, L. Martin, J. Munthe, I. Wängberg, P. Artaxo, F. Morais, H. De Melo Jorge Barbosa, J. Brito, W. Cairns, C. Barbante, M. Del Carmen Diéguez, P. Elizabeth Garcia, D. Aurélien, H. Angot, O. Magand, H. Skov, M. Horvat, J. Kotnik, K. Alana Read, L. Mendes Neves, B. Manfred Gawlik, F. Sena, N. Mashyanov, V. Obolkin, D. Wip, X. Bin Feng, H. Zhang, X. Fu, R. Ramachandran, D. Cossa, J. Knoery, N. Marusczak, M. Nerentorp, C. Norstrom, Atmospheric mercury concentrations observed at ground-based monitoring sites globally distributed in the framework of the GMOS network, Atmos. Chem. Phys. 16 (2016) 11915–11935, https://doi.org/10.5194/acp-16-11915-2016.

[12] G.-R. Sheu, N.-H. Lin, Characterizations of wet mercury deposition to a remote islet (Pengjiayu) in the subtropical Northwest Pacific Ocean, Atmos. Environ. 77 (2013) 474–481, https://doi.org/10.1016/j.atmosenv.2013.05.038.

[13] Gay Sheu, Schmeltz Olson, Chang Lin Nguyen, A new monitoring effort for Asia: the Asia Pacific mercury monitoring network (APMMN), Atmosphere 10 (2019) 481, https://doi.org/10.3390/atmos10090481.

[14] K.A. Pfaffhuber, T. Berg, D. Hirdman, A. Stohl, Atmospheric mercury observations from Antarctica: seasonal variation and source and sink region calculations, Atmos. Chem. Phys. 12 (2012) 3241–3251, https://doi.org/10.5194/acp-12-3241-2012.

[15] F. Slemr, H. Angot, A. Dommergue, O. Magand, M. Barret, A. Weigelt, R. Ebinghaus, E.G. Brunke, K.A. Pfaffhuber, G. Edwards, D. Howard, J. Powell, M. Keywood, F. Wang, Comparison of mercury concentrations measured at several sites in the Southern Hemisphere, Atmos. Chem. Phys. 15 (2015) 3125–3133, https://doi.org/10.5194/acp-15-3125-2015.

[16] F. Slemr, L. Martin, C. Labuschagne, T. Mkololo, H. Angot, O. Magand, A. Dommergue, P. Garat, M. Ramonet, J. Bieser, Atmospheric mercury in the southern hemisphere – Part 1: trend and inter-annual variations in atmospheric mercury at Cape point, South Africa, in 2007–2017, and on Amsterdam island in 2012–2017, Atmos. Chem. Phys. 20 (2020) 7683–7692, https://doi.org/10.5194/acp-20-7683-2020.

[17] H. Angot, M. Barret, O. Magand, M. Ramonet, A. Dommergue, A 2-year record of atmospheric mercury species at a background Southern Hemisphere station on Amsterdam Island, Atmos. Chem. Phys. 14 (2014) 11461–11473, https://doi.org/10.5194/acp-14-11461-2014.

[18] H. Angot, A. Dastoor, F. De Simone, K. Gärdfeldt, C.N. Gencarelli, I.M. Hedgecock, S. Langer, O. Magand, M.N. Mastromonaco, C. Nordstrøm, K.A. Pfaffhuber, N. Pirrone, A. Ryjkov, N.E. Selin, H. Skov, S. Song, F. Sprovieri, A. Steffen, K. Toyota, O. Travnikov, X. Yang, A. Dommergue, Chemical cycling and deposition of atmospheric mercury in polar regions: review of recent measurements and comparison with models, Atmos. Chem. Phys. 16 (2016) 10735–10763, https://doi.org/10.5194/ACP-16-10735-2016.

[19] H. Angot, I. Dion, N. Vogel, M. Legrand, O. Magand, A. Dommergue, Multi-year record of atmospheric mercury at Dumont d'Urville, East Antarctic coast: continental outflow and oceanic influences, Atmos. Chem. Phys. 16 (2016) 8265–8279, https://doi.org/10.5194/ACP-16-8265-2016.

[20] E.-G. Brunke, C. Walters, T. Mkololo, L. Martin, C. Labuschagne, B. Silwana, F. Slemr, A. Weigelt, R. Ebinghaus, V. Somerset, Mercury in the atmosphere and in rainwater at Cape point, South Africa, Atmos, Environ. Times 125 (2016) 24–32, https://doi.org/10.1016/j.atmosenv.2015.10.059.

[21] E.-G. Brunke, R. Ebinghaus, H.H. Kock, C. Labuschagne, F. Slemr, Emissions of mercury in southern Africa derived from long-term observations at Cape Point, South Africa, Atmos. Chem. Phys. 12 (2012) 7465–7474, https://doi.org/10.5194/acp-12-7465-2012.

[22] M.C. Diéguez, M. Bencardino, P.E. García, F. D'Amore, J. Castagna, F. De Simone, C. Soto Cárdenas, S. Ribeiro Guevara, N. Pirrone, F. Sprovieri, A multi-year record of atmospheric mercury species at a background mountain station in Andean Patagonia (Argentina): temporal trends and meteorological influence, Atmos. Environ. 214 (2019), 116819, https://doi.org/10.1016/j.atmosenv.2019.116819.

[23] A.M. Koenig, O. Magand, P. Laj, M. Andrade, I. Moreno, F. Velarde, G. Salvatierra, R. Gutierrez, L. Blacutt, D. Aliaga, T. Reichler, K. Sellegri, O. Laurent, M. Ramonet, A. Dommergue, Seasonal patterns of atmospheric mercury in tropical South America as inferred by a continuous total gaseous mercury record at Chacaltaya station (5240 m) in Bolivia, Atmos. Chem. Phys. 21 (2021) 3447–3472, https://doi.org/10.5194/acp-21-3447-2021.

[24] M. Martino, A. Tassone, L. Angiuli, A. Naccarato, P.R. Dambruoso, F. Mazzone, L. Trizio, C. Leonardi, F. Petracchini, F. Sprovieri, N. Pirrone, F. D'Amore, M. Bencardino, First atmospheric mercury measurements at a coastal site in the Apulia region: seasonal variability and source analysis, Environ. Sci. Pollut. Res. (2022) 16, https://doi.org/10.1007/s11356-022-20505-6.

[25] J. Bieser, H. Angot, F. Slemr, L. Martin, Atmospheric mercury in the southern hemisphere – Part 2: source apportionment analysis at Cape point station, South Africa, Atmos, Chem. Phys. 20 (2020) 10427–10439, https://doi.org/10.5194/acp-20-10427-2020.

[26] A. Gaudry, P. Monfray, G. Polian, G. Bonsang, B. Ardouin, A. Jegou, G. Lambert, Non-seasonal variations of atmospheric CO 2 concentrations at Amsterdam Island, Tellus B Chem. Phys. Meteorol. 43 (1991) 136–143, https://doi.org/10.3402/tellusb.v43i2.15258.

[27] V. Gros, B. Bonsang, D. Martin, P.C. Novelli, V. Kazan, Carbon monoxide short term measurements at Amsterdam island: estimations of biomass burning emission rates, Chemosphere: Global Change Sci. 1 (1999) 163–172, https://doi.org/10.1016/S1465-9972(99)00009-4.

[28] V. Gros, B. Bonsang, R. Sarda Esteve, Atmospheric carbon monoxide 'in situ' monitoring by automatic gas chromatography, Chemosphere: Global Change Sci. 1 (1999) 153–161, https://doi.org/10.1016/S1465-9972(99)00010-0.

[29] M. Jiskra, J.E. Sonke, D. Obrist, J. Bieser, R. Ebinghaus, C.L. Myhre, K.A. Pfaffhuber, I. Wängberg, K. Kyllönen, D. Worthy, L.G. Martin, C. Labuschagne, T. Mkololo, M. Ramonet, O. Magand, A. Dommergue, A vegetation control on seasonal variations in global atmospheric mercury concentrations, Nat. Geosci. 11 (2018) 244–250, https://doi.org/10.1038/s41561-018-0078-8.

[30] C. Yver-Kwok, C. Philippon, P. Bergamaschi, T. Biermann, F. Calzolari, H. Chen, S. Conil, P. Cristofanelli, M. Delmotte, J. Hatakka, M. Heliasz, O. Hermansen, K. Kominkova, D. Kubistin, N. Kumps, O. Laurent, T. Laurila, I. Lehner, J. Levula, M. Lindauer, M. Lopez, I. Mammarella, G. Manca, P. Marklund, J.M. Metzger,

M. Mölder, S.M. Platt, M. Ramonet, L. Rivier, B. Scheeren, M. Kumar Sha, P. Smith, M. Steinbacher, G. Vítková, S. Wyss, Evaluation and optimization of ICOS atmosphere station data as part of the labeling process, Atmos. Meas. Tech. 14 (2021) 89–116, https://doi.org/10.5194/AMT-14-89-2021.
[31] S.D. Chambers, S. Preunkert, R. Weller, S.-B. Hong, R.S. Humphries, L. Tositti, H. Angot, M. Legrand, A.G. Williams, A.D. Griffiths, J. Crawford, J. Simmons, T. J. Choi, P.B. Krummel, S. Molloy, Z. Loh, I. Galbally, S. Wilson, O. Magand, F. Sprovieri, N. Pirrone, A. Dommergue, Characterizing atmospheric transport pathways to Antarctica and the remote southern ocean using radon-222, Front. Earth Sci. 6 (2018) 1–28, https://doi.org/10.3389/feart.2018.00190.
[32] A. Gaudry, G. Polian, B. Ardouin, G. Lambert, Radon-calibrated emissions of CO_2 from South Africa, Tellus B Chem. Phys. Meteorol. 42 (1990) 9–19, https://doi.org/10.3402/tellusb.v42i1.15187.
[33] L. Harrison, C. Funk, A. McNally, S. Shukla, G. Husak, Pacific sea surface temperature linkages with Tanzania's multi-season drying trends, Int. J. Climatol. 39 (2019) 3057–3075, https://doi.org/10.1002/joc.6003.
[34] F. D'Amore, M. Bencardino, S. Cinnirella, F. Sprovieri, N. Pirrone, Data quality through a web-based QA/QC system: implementation for atmospheric mercury data from the global mercury observation system, Environ. Sci. Process. Impacts. 17 (2015) 1482–1491, https://doi.org/10.1039/c5em00205b.
[35] A. Tassone, S. Moretti, M. Martino, N. Pirrone, F. Sprovieri, A. Naccarato, Modification of the EPA method 1631E for the quantification of total mercury in natural waters, MethodsX 7 (2020), 100987, https://doi.org/10.1016/j.mex.2020.100987.
[36] GMOS, Method for the determination of total mercury in precipitation, GMOS (2011) 1–22.
[37] O. Magand, A. Dommergue, Continuous Measurements of Atmospheric Mercury at Amsterdam Island (L2), Aeris., 2021. https://dx.doi.org/10.25326/168.
[38] P.K. Sen, Estimates of the regression coefficient based on Kendall's Tau, J. Am. Stat. Assoc. 63 (1968) 1379, https://doi.org/10.2307/2285891.
[39] M.J. McGill, R.J. Swap, J.E. Yorks, P.A. Selmer, S.J. Piketh, Observation and quantification of aerosol outflow from southern Africa using spaceborne lidar, South Afr. J. Sci. 116 (2020) 65–70, https://doi.org/10.17159/sajs.2020/6398.
[40] E. Baboukas, J. Sciare, N. Mihalopoulos, Spatial, temporal and interannual variability of methanesulfonate and non-sea-salt sulfate in rainwater in the southern Indian ocean (Amsterdam, Crozet and Kerguelen islands), J. Atmos. Chem. 48 (2004) 35–57, https://doi.org/10.1023/B:JOCH.0000034508.13326.cd.
[41] R.R. Draxler, G.D. Rolph, HYSPLIT (HYbrid Single-Particle Lagrangian Integrated Trajectory), NOAA Air Resour. Lab. Coll. Park. MD, 2003. http://www.arl.noaa.gov/ready/hysplit4.html. (Accessed 3 May 2022). accessed.
[42] J.L. Moody, P.J. Samson, The influence of atmospheric transport on precipitation chemistry at two sites in the midwestern United States, Atmos, Environ. Times 23 (1989) 2117–2132, https://doi.org/10.1016/0004-6981(89)90173-X.
[43] J.H. Ward, Hierarchical Grouping to optimize an objective function, J. Am. Stat. Assoc. 58 (1963) 236–244.
[44] M.S. Landis, G.J. Keeler, Atmospheric mercury deposition to lake Michigan during the lake Michigan mass balance study, Environ. Sci. Technol. (2002), https://doi.org/10.1021/es011217b.
[45] D.S. Wilks, Statistical Methods in the Atmospheric Sciences, Fourth, Elsevier, Oxford, 2019, https://doi.org/10.1016/C2017-0-03921-6.
[46] M. Anjos, A.C. Targino, P. Krecl, G.Y. Oukawa, R.F. Braga, Analysis of the urban heat island under different synoptic patterns using local climate zones, Build. Environ. 185 (2020), 107268, https://doi.org/10.1016/J.BUILDENV.2020.107268.
[47] R.R. Draxler, HYSPLIT4 User 's Guide, Silver Spring, USA, 1999. http://www.arl.noaa.gov/hysplit.html.
[48] Z.L. Fleming, P.S. Monks, A.J. Manning, Review: untangling the influence of air-mass history in interpreting observed atmospheric composition, Atmos. Res. 104–105 (2012) 1–39. https://doi.org/10.1016/j.atmosres.2011.09.009.
[49] N. Pekney, C. Davidson, L. Zhou, P. Hopke, Application of PSCF and CPF to PMF-modeled sources of PM2.5 in Pittsburgh, in: Aerosol Sci. Technol., 2006, pp. 952–961, https://doi.org/10.1080/02786820500543324.
[50] K.R. Travis, C.L. Heald, H.M. Allen, E.C. Apel, S.R. Arnold, D.R. Blake, W.H. Brune, X. Chen, R. Commane, J.D. Crounse, B.C. Daube, G.S. Diskin, J.W. Elkins, M. J. Evans, S.R. Hall, E.J. Hintsa, R.S. Hornbrook, P.S. Kasibhatla, M.J. Kim, G. Luo, K. McKain, D.B. Millet, F.L. Moore, J. Peischl, T.B. Ryerson, T. Sherwen, A. B. Thames, K. Ullmann, X. Wang, P.O. Wennberg, G.M. Wolfe, F. Yu, Constraining remote oxidation capacity with ATom observations, Atmos. Chem. Phys. 20 (2020) 7753–7781, https://doi.org/10.5194/acp-20-7753-2020.
[51] D.P. Edwards, L.K. Emmons, J.C. Gille, A. Chu, J.L. Attié, L. Giglio, S.W. Wood, J. Haywood, M.N. Deeter, S.T. Massie, D.C. Ziskin, J.R. Drummond, Satellite-observed pollution from Southern Hemisphere biomass burning, J. Geophys. Res. Atmos. 111 (2006) 1–17, https://doi.org/10.1029/2005JD006655.
[52] M.A.K. Khalil, R.A. Rasmussen, Sources, sinks, and seasonal cycles of atmospheric methane, J. Geophys. Res. Ocean. 88 (1983) 5131–5144, https://doi.org/10.1029/JC088iC09p05131.
[53] M.A.K. Khalil, R.A. Rasmussen, The global cycle of carbon monoxide: trends and mass balance, Chemosphere 20 (1990) 227–242, https://doi.org/10.1016/0045-6535(90)90098-E.
[54] J. Williams, V. Gros, B. Bonsang, V. Kazan, HO cycle in 1997 and 1998 over the southern Indian Ocean derived from CO, radon, and hydrocarbon measurements made at Amsterdam Island, J. Geophys. Res. Atmos. 106 (2001) 12719–12725, https://doi.org/10.1029/2001JD900116.
[55] E.-G. Brunke, C. Labuschagne, B. Parker, H.E. Scheel, S. Whittlestone, Baseline air mass selection at Cape Point, South Africa: application of 222Rn and other filter criteria to CO2, Atmos. Environ. 38 (2004) 5693–5702, https://doi.org/10.1016/j.atmosenv.2004.04.024.
[56] D.S. McLagan, C.P.J. Mitchell, A. Steffen, H. Hung, C. Shin, G.W. Stupple, M.L. Olson, W.T. Luke, P. Kelley, D. Howard, G.C. Edwards, P.F. Nelson, H. Xiao, G. R. Sheu, A. Dreyer, H. Huang, B. Abdul Hussain, Y.D. Lei, I. Tavshunsky, F. Wania, Global evaluation and calibration of a passive air sampler for gaseous mercury, Atmos. Chem. Phys. 18 (2018) 5905–5919, https://doi.org/10.5194/acp-18-5905-2018.
[57] J.A. Fisher, P.F. Nelson, Atmospheric mercury in Australia, Elem. Sci. Anthr. 8 (2020) 1–20, https://doi.org/10.1525/elementa.2020.070.
[58] C. Liu, X. Liao, J. Qiu, Y. Yang, X. Feng, R.P. Allan, N. Cao, J. Long, J. Xu, Observed variability of intertropical convergence zone over 1998-2018, Environ. Res. Lett. 15 (2020), https://doi.org/10.1088/1748-9326/aba033.
[59] H. Lashkari, M. Jafari, Annual displacement and appropriate index to determine ITCZ position in East Africa and the Indian Ocean regions, Meteorol. Atmos. Phys. 133 (2021) 1111–1126, https://doi.org/10.1007/s00703-021-00797-y.
[60] G. Liu, Y. Cai, N. O'Driscoll, Environmental Chemistry and Toxicology of Mercury, 2011, https://doi.org/10.1002/9781118146644.
[61] Y.-S. Seo, Y.-J. Han, H.-D. Choi, T.M. Holsen, S.-M. Yi, Characteristics of total mercury (TM) wet deposition: scavenging of atmospheric mercury species, Atmos. Environ. 49 (2012) 69–76, https://doi.org/10.1016/j.atmosenv.2011.12.031.
[62] X. Fu, X. Yang, X. Lang, J. Zhou, H. Zhang, B. Yu, H. Yan, C.J. Lin, X. Feng, Atmospheric wet and litterfall mercury deposition at urban and rural sites in China, Atmos. Chem. Phys. 16 (2016) 11547–11562, https://doi.org/10.5194/acp-16-11547-2016.
[63] V. Shah, D.J. Jacob, C.P. Thackray, X. Wang, E.M. Sunderland, T.S. Dibble, A. Saiz-Lopez, I. Cernusák, V. Kellö, P.J. Castro, R. Wu, C. Wang, Improved mechanistic model of the atmospheric redox chemistry of mercury, Environ. Sci. Technol. 55 (2021) 14445–14456, https://doi.org/10.1021/acs.est.1c03160.
[64] H.M. Horowitz, D.J. Jacob, Y. Zhang, T.S. Dibble, F. Slemr, H.M. Amos, J.A. Schmidt, E.S. Corbitt, E.A. Marais, E.M. Sunderland, A new mechanism for atmospheric mercury redox chemistry: implications for the global mercury budget, Atmos. Chem. Phys. 17 (2017) 6353–6371, https://doi.org/10.5194/acp-17-6353-2017.
[65] O. Travnikov, H. Angot, P. Artaxo, M. Bencardino, J. Bieser, F. D'Amore, A. Dastoor, F. De Simone, M.C. Diéguez, A. Dommergue, R. Ebinghaus, X. Bin Feng, C. N. Gencarelli, I.M. Hedgecock, O. Magand, L. Martin, V. Matthias, N. Mashyanov, N. Pirrone, R. Ramachandran, K. Alana Read, A. Ryjkov, N.E. Selin, F. Sena, S. Song, F. Sprovieri, D. Wip, I. Wängberg, X. Yang, Multi-model study of mercury dispersion in the atmosphere: atmospheric processes and model evaluation, Atmos. Chem. Phys. 17 (2017) 5271–5295, https://doi.org/10.5194/acp-17-5271-2017.
[66] R.V. Rohli, A.J. Vega, Climatology, Jones & Bartlett Learning, 2015.
[67] F. Slemr, C.A. Brenninkmeijer, A. Rauthe-Schöch, A. Weigelt, R. Ebinghaus, E. Brunke, L. Martin, T.G. Spain, S. O'Doherty, El Niño–Southern Oscillation influence on tropospheric mercury concentrations, Geophys. Res. Lett. 43 (2016) 1766–1771, https://doi.org/10.1002/2016GL067949.
[68] R.A. Preston-Whyte, P.D. Tyson, Atmosphere and Weather of Southern Africa, Oxford University Press, 1988. https://agris.fao.org/agris-search/search.do?recordID=US201300685112. (Accessed 19 November 2021). accessed.
[69] F. Carbone, M.S. Landis, C.N. Gencarelli, A. Naccarato, F. Sprovieri, F. De Simone, I.M. Hedgecock, N. Pirrone, Sea surface temperature variation linked to elemental mercury concentrations measured on Mauna Loa, Geophys. Res. Lett. (2016), https://doi.org/10.1002/2016GL069252.

[70] L.S.P. Nguyen, K.T. Nguyen, S.M. Griffith, G.R. Sheu, M.C. Yen, S.C. Chang, N.H. Lin, Multiscale temporal variations of atmospheric mercury distinguished by the Hilbert–Huang transform analysis reveals multiple El Niño–southern Oscillation Links, Environ. Sci. Technol. 56 (2022) 1423–1432, https://doi.org/10.1021/acs.est.1c03819.
[71] S. Huang, Y. Zhang, Interannual variability of air-sea exchange of mercury in the global ocean: the "seesaw effect" in the equatorial Pacific and contributions to the atmosphere, Environ. Sci. Technol. 55 (2021) 7145–7156, https://doi.org/10.1021/acs.est.1c00691.
[72] G. Polian, G. Lambert, B. Ardouin, A. Jegou, Long-range transport of continental radon in subantarctic and antarctic areas, Tellus B Chem. Phys. Meteorol. 38 (1986) 178–189, https://doi.org/10.3402/tellusb.v38i3-4.15126.
[73] C. deW. Rautenbach, I. Smith, Teleconnections between global sea-surface temperatures and the interannual variability of observed and model simulated rainfall over southern Africa, J. Hydrol. 254 (2001) 1–15, https://doi.org/10.1016/S0022-1694(01)00454-1.
[74] J.M. Miller, J.L. Moody, J.M. Harris, A. Gaudry, A 10-year trajectory flow climatology for Amsterdam Island, 1980–1989, Atmos, Environ. Times Part A. Gen. Top. 27 (1993) 1909–1916, https://doi.org/10.1016/0960-1686(93)90296-B.
[75] M. Ramonet, J.C. Le Roulley, P. Bousquet, P. Monfray, Radon-222 measurements during the tropoz II campaign and comparison with a global atmospheric transport model, J. OfAtmospheric Chem. 23 (1996) 107–136.